



Attenuation Correction for Dedicated Cardiac SPECT Imaging Without Using Transmission Data

Transmisyon Verilerini Kullanmadan Özel Kardiyak SPECT Görüntülemeye Atenüasyon Düzeltmesi

© Getu Ferenji Tadesse^{1,2,3}, © Parham Geramifar⁴, © Mehrshad Abbasi⁵, © Eyachew Misganew Tsegaw⁶, © Mohammad Amin⁷, © Ali Salimi², © Mohammad Mohammadi², © Behnoosh Teimourianfard⁸, © Mohammed Reza Ay^{1,2}

¹Research Center for Molecular and Cellular Imaging (RCMCI), Advanced Medical Technologies and Equipment Institute (AMTEI), Tehran University of Medical Sciences (TUMS), Tehran, Iran

²Department of Medical Physics and Biomedical Engineering, Tehran University of Medical Sciences, Tehran, Iran

³St. Paul's Hospital Millennium Medical College, Department of Internal Medicine, Addis Ababa, Ethiopia

⁴Tehran University of Medical Sciences, Shariati Hospital, Research Center for Nuclear Medicine, Tehran, Iran

⁵Tehran University of Medical Sciences, Department of Nuclear Medicine, Vali-Asr Hospital, Tehran, Iran

⁶Debre Tabor University Faculty of Natural and Computational Sciences, Department of Physics, Debre Tabor, Ethiopia

⁷Shahed University Faculty of Science, Department of Computer Science, Tehran, Iran

⁸Tehran University of Medical Sciences, Postdoctoral Research Fellow, Tehran, Iran

Abstract

Objectives: Attenuation correction (AC) using transmission scanning-like computed tomography (CT) is the standard method to increase the accuracy of cardiac single-photon emission computed tomography (SPECT) images. Recently developed dedicated cardiac SPECT do not support CT, and thus, scans on these systems are vulnerable to attenuation artifacts. This study presented a new method for generating an attenuation map directly from emission data by segmentation of precisely non-rigid registration extended cardiac-torso (XCAT)-digital phantom with cardiac SPECT images.

Methods: In-house developed non-rigid registration algorithm automatically aligns the XCAT- phantom with cardiac SPECT image to precisely segment the contour of organs. Pre-defined attenuation coefficients for given photon energies were assigned to generate attenuation maps. The CT-based attenuation maps were used for validation with which cardiac SPECT/CT data of 38 patients were included. Segmental myocardial counts of a 17-segment model from these databases were compared based on the basis of the paired t-test.

Results: The mean, and standard deviation of the mean square error and structural similarity index measure of the female stress phase between the proposed attenuation maps and the CT attenuation maps were $6.99 \pm 1.23\%$ and $92 \pm 2.0\%$, of the male stress were $6.87 \pm 3.8\%$ and $96 \pm 1.0\%$. Proposed attenuation correction and computed tomography based attenuation correction average myocardial perfusion count was significantly higher than that in non-AC in the mid-inferior, mid-lateral, basal-inferior, and lateral regions ($p < 0.001$).

Conclusion: The proposed attenuation maps showed good agreement with the CT-based attenuation map. Therefore, it is feasible to enable AC for a dedicated cardiac SPECT or SPECT standalone scanners.

Keywords: Attenuation correction, cardiac, SPECT/CT, XCAT, emission data

Öz

Amaç: Transmisyon taraması benzeri bilgisayarlı tomografi (BT) kullanan atenüasyon düzeltmesi (AC), kardiyak tek foton emisyonlu bilgisayarlı tomografi (SPECT) görüntülerinin doğruluğunu artırmada standart yöntemdir. Son zamanlarda geliştirilen özel kardiyak SPECT BT'yi

Address for Correspondence: Prof. Mohammed Reza Ay MD, Research Center for Molecular and Cellular Imaging (RCMCI), Advanced Medical Technologies and Equipment Institute (AMTEI), Tehran University of Medical Sciences (TUMS); Department of Medical Physics and Biomedical Engineering, Tehran University of Medical Sciences, Tehran, Iran

Phone: +989125789765 **E-mail:** mohammadreza_ay@tums.ac.ir ORCID ID: <https://orcid.org/0000-0001-5356-0894>

Received: 01.03.2022 **Accepted:** 02.06.2022

©Copyright 2023 by Turkish Society of Nuclear Medicine
Molecular Imaging and Radionuclide Therapy published by Galenos Yayınevi.

desteklememektedir ve bu nedenle, bu sistemlerdeki taramalar atenüasyon artefaktlarına karşı savunmasızdır. Bu çalışmada, kardiyak SPECT görüntüleri ile birlikte rijit olmayan kayıt genişletilmiş kardiyak-gövde (XCAT)-dijital fantomun segmentasyonu yoluyla doğrudan emisyon verilerinden bir atenüasyon haritası oluşturmak için yeni bir yöntem sunulmaktadır.

Yöntem: Kendi geliştirdiğimiz rijit olmayan kayıt algoritması, organların dış hatlarını hassas şekilde bölümlere ayırmak için XCAT-fantomunu kardiyak SPECT görüntüsüyle otomatik olarak hizalar. Atenüasyon haritaları oluşturmak için verilen foton enerjileri için önceden tanımlanmış atenüasyon katsayıları atanmıştır. Otuz sekiz hastanın kardiyak SPECT/CT verilerinin dahil edildiği doğrulama için CT tabanlı atenüasyon haritaları kullanıldı. Bu veritabanlarından alınan 17 segmentli bir modelin segmental miyokardiyal sayımları, eşleştirilmiş örneklem t-testi ile karşılaştırıldı.

Bulgular: Önerilen atenüasyon haritaları ile CT atenüasyon haritaları arasındaki kadın stres fazının ortalama kare hatası ve benzerlik indeksi ölçüsü yapısal benzerlik indeksi ölçümünün ortalama ve standart sapması sırasıyla $6,99 \pm 1,23$ ve $92 \pm 2,0$ iken, erkek stres fazının değerleri $6,87 \pm 3,8$ ve $96 \pm 1,0$ idi. Mid-inferior, mid-lateral, bazal-inferior ve lateral bölgelerde ProAC ve CTAC ortalama miyokardiyal perfüzyon sayısı non-AC'ye göre anlamlı olarak yüksekti ($p < 0,001$).

Sonuç: Önerilen atenüasyon haritaları BT tabanlı atenüasyon haritasıyla iyi bir uyum gösterdi. Böylelikle, kardiyak çalışmalar özel SPECT veya sadece SPECT tarayıcıları için AC'yi etkinleştirmek mümkün olmuştur.

Anahtar kelimeler: Atenüasyon düzeltmesi, kardiyak, SPECT/BT, XCAT, emisyon verileri

Introduction

Single-photon emission computed tomography (SPECT) is a non-invasive molecular imaging technique that can deliver the radio-tracer distribution images in the patient body by detecting gamma-ray photons (1). Photon attenuation is the most physical factor artifact that contributes to the quantitative and qualitative inaccuracy in cardiac SPECT and can lead to misinterpretation of images by the physicians (2). Thus, attenuation correction (AC) is important for reducing uncertainty in cardiac diagnosis.

van Dijk et al. (3) reported that after the implementation of cardiac AC, images interpreted as "normal" increased from 45 to 72% and the total images that are unequivocal went from 57 to 80%. Moreover, accurate cardiac AC can enhance in "true-positive" and significantly decrease in "false positive" results as confirmed by invasive coronary angiography, hence increase the diagnostic positive predictive value (4).

Non-uniform AC is obtained by measuring the attenuation distribution map in the patient's body, which can then be used along with iterative reconstruction algorithms to accurately compensate for the variable attenuation in the chest. Therefore, to ascertain the accurate correction, which in turn modifies the intensity of the cardiac image, it is essential to create a patient-specific attenuation map (5,6,7,8,9).

There are two methods for generating non-homogeneous attenuation map for AC of SPECT data: transmission-less method and transmission-based scanning using an external radionuclide or X-ray computed tomography (CT). The use of hybrid SPECT/CT systems and for generating non-homogeneous attenuation map is the most conventionally effective method. However, these systems are significantly more expensive than SPECT-only systems and need

larger imaging housings and further room lead shielding. Additionally, it increases the radiation exposure dose to the patients and misregistration between emission and transmission data can occur due to patient motion. According to the study (10) conducted with the myocardial perfusion SPECT/CT for 509 patients, the mean volume computed tomography dose index ($CTDI_{vol}$) received from attenuation CT was 1.34 ± 0.19 mGy. Moreover, most of the systems used for cardiac imaging are either dedicated to cardiac scans that do not support transmission scanning or SPECT standalone due to the high cost of SPECT/CT (11). Around 80% of SPECT market share is stand-alone SPECT systems (12,13) and AC for these systems has paramount importance.

Currently, dedicated cardiac scanners have been developed by different vendor including a dedicated cardiac SPECT (called ProSPECT) with two detectors fixed 90° developed in our lab (Parto Negar Persia Co., Tehran, Iran) (14,15). The ProSPECT system is introduced as an optimized and low-cost design in nuclear cardiology. The gantry and table of the system are designed to comfortably accommodate patients and to provide dual patients positioning (supine and prone). We expect the major benefit of this research is to increase the diagnostic accuracy for such systems and the ~80% SPECT-only scanners to provide a healthy center community with the benefit of convenient and improved image quality.

Generally, there are three techniques for generating attenuation maps from SPECT emission data only. The first technique includes the segmentation of either the photopeak or the scatter data to generate the attenuation map (9,16,17,18,19). A coarse attenuation map can be obtained by segmenting different regions in SPECT images and assigning pre-defined attenuation coefficients. However, these methods are faced difficulty in defining

body outline and organs contour accurately from SPECT emission data. The second technique for generating an attenuation map is model-based methods that estimate the attenuation coefficients directly from the emission data (20,21,22,23,24). However, these models use simultaneous estimating SPECT emission and attenuation parameters; there were crosstalk between emission and attenuation parameters, and thus are inaccurate enough. These methods also suffer from high computation time and were applied only in a slice-by-slice manner. The third and recent technique is deep learning-based approaches that have been proposed to estimate images of one modality from those of another (1). CT attenuation maps were generated from SPECT data alone. This method though, it is more effective than the previous two technique; however, it requires a very large amount of data from another model to perform better than other techniques. It is extremely expensive to train due to complex data models, requiring expensive GPUs and hundreds of machines. This increases the cost to the users.

In this paper, we demonstrated that non-uniform attenuation map was generated from semi-automatic non-rigid registration of an emission reconstructed image with an extended cardiac-torso (XCAT) digital phantom (25) using an in-house developed algorithm and segmenting tissues to assign the respective linear attenuation coefficient to accurately correct the attenuation of the photons passing through the patient body. The use of a proposed map (ProMap) for the AC of the clinical data was evaluated, and the results were compared with CT-based attenuation map (CTMap). This study presented a new method for generating an attenuation map for cardiac AC directly from emission data by segmentation of precisely non-rigid registration XCAT-digital phantom with cardiac SPECT image.

Materials and Methods

This study included the following steps: a) generating the proposed attenuation map, b) developing a maximum-likelihood expectation-maximization (MLEM) algorithm for image reconstruction using MATLAB script (MATLAB 2019a version) and implementation of AC based on the proposed attenuation map, and c) clinical validation of the proposed method.

Ethics Committee Approval

The Tehran University of Medical Sciences Tehran, Iran, Vice-chancellor in research affairs approved the study protocol (approval ID: IR.TUMS.VCR.REC.1397.6355, date: 27.11.2018). All patients gave their informed consent before inclusion in the study.

Development of an Algorithm for Generating an Attenuation Map

The proposed attenuation map was synthesized by the segmentation of non-rigid registering of the simulated 3D XCAT digital phantom with the cardiac SPECT reconstructed image. The XCAT software includes a pair of highly detailed male and female anatomies defined using non-uniform rational B-spline and segmentation of the visible male and female anatomical patient datasets (25,26,27). XCAT non-rigid registration with emission image-based AC methods consist of differentiating the regions with different attenuation properties, assigning the pre-defined linear attenuation coefficients to them, and using the resultant attenuation map to correct the SPECT emission data during reconstruction.

The XCAT phantom is gained widespread importance in the low-resolution nuclear medicine imaging research and lacks the anatomical detail required for use in higher-resolution imaging modalities such as X-ray CT. Moreover, it has paramount importance for improving imaging instrumentation, data acquisition, techniques, image reconstruction, and processing methods, which in turn lead to enhance image quality and more accurate clinical diagnosis (28).

The in-house non-rigid registration algorithm developed in the MATLAB environment was used to perform automatically non-rigid registration of the simulated XCAT phantom of the thorax region with the SPECT image. Generally, the process of non-rigid registration involved in this study was finding the optimal geometric transformation that maximizes the correspondences across the simulated XCAT digital phantom and the SPECT reconstructed image.

The proposed attenuation map generated from non-rigid registration of emission image and simulated images were compared with the X-ray CT-based attenuation map by calculating similarity matrices such as root mean square, root mean square error (MSE), mean absolute error and similarity index measure (SSIM).

Generally, the procedure of generating the attenuation map involves the following: first, XCAT simulation for both male and females was performed. Second, matching the body outline was performed for the emission-reconstructed image and simulated XCAT phantom by non-rigid registration of slice by slice for the transversal view, and magnification parameters were used to fit the XCAT size with different sizes patients. Third, after the XCAT images were registered with the preliminary SPECT images, the thoracic region was segmented into soft tissue, lung, and bone. Fourth, according to the report by Okuda et al. (29), attenuation coefficients of 0.280/cm, 0.150/cm, and

0.053/cm were applied for segmented bone, soft tissue, and lung regions, respectively, for the gamma energy of 140 keV.

Development of the MLEM Algorithm

AC gets wide acceptance in routine clinics due to new reconstruction algorithms mentioned together as iterative algorithms (5,30,31,32). Iterative reconstruction algorithms offer a wide-ranging mathematical framework that allows the modeling of physical processes such as attenuation, scatter, and noise characteristics from the emission and detection processes (33). We adopted the ray-driven projector-backprojector technique, which integrates AC as described by Gullberg et al. (34).

System Matrix and Implementation of Attenuation Correction

The ultimate solution to the non-homogeneous attenuation problem in cardiac SPECT imaging could be solved using an iterative algorithm with a projector-backprojector that models the attenuation of photons along with projection and backprojection rays and that calculates attenuation factors for each pixel along each ray from the predetermined attenuation distribution (8,34). The system matrix or projection operator A has a vital role in the quality of the reconstructed images. Each element $A(i,j)$ gives the contribution of photons emitted from the j 'th image voxel in i 'th measurement, which is detected by a specified detector's pixel in a certain position. There are several methods to approximate these contributions and even it is possible to use an unmatched projector-backprojector operator pair. Here, we assumed a matched projector and back-projector operator and determined the contributions by calculating the intersection volume of each ray with each pixel. Considering the parallel hole collimator geometry, each intersection was calculated by finding the intersected area of each ray and pixels, then multiplying it by the slice thickness. The intersection point of each ray's side with each pixel is found and the area of the intersected polygon was calculated. Considering the relatively low resolution of nuclear medicine imaging and a small number of measurements, and the scarcity of the system matrix, we could calculate the system matrix once and store it on memory. Meanwhile the intersection area being calculated, the centroid of each polygon is found, and the distance between the centroid and the ray's detector was also calculated. For each ray, after finding the distance of all contributing pixels, the pixel's indices were sorted regarding their distance to the detector and then cumulative attenuation between the detector and each pixel was found. Then, the exponential correction is applied to the intersected volume and the final system

matrix was obtained. Based on this concept, the system matrix of SPECT was calculated using a MATLAB code. For the image reconstruction, A is a matrix of $M \times N$, where N is the number of pixels, n^2 and $M = NpD$ being the total number of projections of all detector elements, D , of the detector array in all projection directions, Np . It is in this system that one includes the physics of imaging.

Clinical Validation

Study Protocol

To validate the proposed AC method, 38 subjects underwent 2-d Tc-99m-sestamibi stress-rest imaging protocol both normal and abnormal (17 males and 21 females, mean age 55 ± 8 years, range 30-70) who were referred to our center for MPI for assessing coronary artery disease (CAD) were included. The mean body mass index was 26.2 ± 3.7 kg/m² (range, 19.1-31.0 kg/m²). Twenty participants (52.6%) underwent exercise, and 18 (47.4%) underwent pharmacological stress and rest studies. All patients underwent a standard MPI SPECT/CT scanner (Siemens Medical Solutions, Erlangen, Germany). In the pharmacological stress testing, stress was induced by the infusion of either dipyridamole at a rate of $140 \mu\text{g}^{-1} \cdot \text{min}^{-1}$ for 4 min or of dobutamine with escalating $5 \mu\text{g}^{-1} \cdot \text{kg}^{-1} \cdot \text{min}^{-1}$ doses up to $40 \mu\text{g}^{-1} \cdot \text{kg}^{-1} \cdot \text{min}^{-1}$. A standard dose of 750-900 MBq of Tc-99m sestamibi was injected 4 min after dipyridamole injection or at peak heart rate during dobutamine pharmacological stress and rest tests. Emission data were acquired by the use of parallel-hole, low-energy, high-resolution collimator, with the patient in the supine position. The acquisition orbits were circular over 180° arc (45° right anterior oblique to 45° left posterior oblique) with 32 steps (64 views), and emission data were acquired for 20 s per projection. The image acquisition matrix was, 64×64 and the pixel size was 6.4 mm. Images were acquired on the 140 keV photopeak with a 15% (129-151 keV) symmetrical window. Immediately after the acquisition of SPECT images for both stress and rest, CT imaging was performed for generating attenuation maps. CT scanning was performed using 140 kVp and 70 mAs in a 512×512 matrix (1.105 mm per pixel), with 5 mm slice thickness. The total acquisition time for the transmission study was 30 s.

The linear attenuation coefficient measured with CT is calculated at the X-ray energy. Rather than at the energy of the photon emitted by the radiopharmaceutical acquired during the radionuclide imaging study. It is therefore necessary to convert the linear attenuation coefficients obtained from the CT scan to match the energy of the radionuclide used in SPECT acquisitions. This is typically accomplished using the bilinear scaling method, relating

the μ value at the desired energy to the CT number measured at the effective energy of CT X-rays (35). The bilinear scaling method determines μ values via bilinear calibration lines, which are delimited at a CT number of zero Hounsfield units (HU) and are most commonly used in SPECT/CT scanners. This is performed using the system as designed by the manufacture (Siemens HealthCare).

For the administered activity of 750-900 MBq for SPECT and 0.9 mGy $CTDI_{vol}$. For CT, the mean effective doses for the patients considered in this study were 9 mSv for SPECT/CT, from this around 8 mSv for SPECT only. The effective dose for CT can be calculated using dose length product (DLP). It is the $CTDI_{vol}$ multiplied by the length of the scan. The units are mGy centimeters (mGy cm). The DLP can be used to calculate a rough estimate of the effective dose, and the effective dose for SPECT can be estimated using the activity-injected dose.

Patient Studies-reconstruction

Patients' data were reconstructed using an in-house developed MLEM (15 iterations) with and without AC and imported to Cardiac SPECT image reconstruction software (QPS/QGS, Cedars-Sinai Medical Center, Los Angeles, CA, USA) for quantitative analysis and to display standard short-axis, vertical, and horizontal long-axis views and polar maps. Scatter correction was performed on emission projection data obtained from the 15% lower scatter window. Two separate energy windows for the acquisition of the photopeak and the lower scatter according to the standard clinical protocol for Tc-99m (140 keV) were used for the scatter correction. The window widths were both set to 15% as recommended by the manufacturer (Siemens Healthcare), resulting in 108-129 keV for the lower scatter window and 129-151 keV for the photopeak window (36). Reconstructed stress and rest images were smoothed using a 3-dimensional Butterworth low-pass filter with a cutoff frequency 0.4 Hz with an order of 8.0. For AC, two different density maps were used: an attenuation map generated from the transmission study (CTMap) where the μ values were calculated from the CT numbers obtained (HU) and the ProMap generated from the emission data.

For the validation of the AC with ProMap, a QPS software algorithm was used to generate perfusion polar maps of 17 segments. Moreover, total counts of each segment attenuation corrected using ProMap and CTMap, were compared by paired t-test. Proposed attenuation correction (ProAC), computed tomography based attenuation correction (CTAC), and non-attenuation correction (NAC) databases were calculated on the basis of the QPS software for both genders.

Quantitative Evaluation

Percent of Variability and Relative Error

To quantitatively assess the homogeneity of radiotracer distribution in patient's image and the improvement inhomogeneity with AC, circumferential count profiles were generated from the apical, midventricular, and basal slices of NAC, ProAC, and CTAC. Image uniformity was assessed by the percentage variability (PV) of the count profiles defined by the following (11):

$$PV = \frac{SD}{Mean} \times 100 \quad (1)$$

where standard deviation (SD) and mean denote the values of the count profiles for each slice. For all slices, the mean percent variability can be calculated as follows:

$$MeanPV = \frac{1}{3} \sum_{i=1}^3 \frac{SD(i)}{Mean(i)} \times 100 \quad (2)$$

where SD (i) and mean (i) denote the values of the count profiles for slice i (1, apical; 2, midventricle; and 3, basal).

We also used percentage of relative error (RE%) in the 17 segmented regions of the perfusion polar map between our proposed AC and the reference CTAC images:

$$RE\% = \frac{ProAC - CTAC}{CTAC} \times 100 \quad (3)$$

The results of the comparative analysis are shown using box plots. In these plots, the box shows the median (horizontal line), with the lower (Q1) and upper quartiles (Q3) define the 25th and 75th percentiles, respectively.

Moreover, the proposed attenuation maps were then compared with the CT-based attenuation maps in terms of Voxelwise MSE and SSIM.

$$MSE = \frac{1}{vxl} \sum_{v=1}^{vxl} (ProMap(v) - CTMap(v))^2 \quad (4)$$

$$SSIM = \frac{(2Ave_{ProMap}Ave_{CTMap} + c_1)(2\delta_{ProMap,CTMap} + c_2)}{(Ave_{ProMap}^2 + Ave_{CTMap}^2 + c_1)(\delta_{ProMap}^2 + \delta_{CTMap}^2 + c_2)} \quad (5)$$

Where vxl stands for voxel, ProMap is the proposed attenuation map, and CTMap is CT-based attenuation map. In Equation (6), Ave_{ProMap} and Ave_{CTMap} stand for the mean value of the proposed attenuation map and CT-based attenuation map, respectively. δ_{ProMap}^2 and δ_{CTMap}^2 denote the variances of ProMap and CTMap, respectively, and $\delta_{ProMap,CTMap}$ the covariance of ProMap and CTMap images, respectively. The constants ($C1$: 0.01 and $C2$: 0.02) were set to avoid division by insignificant values.

Statistical Analysis

The proposed attenuation maps were further applied for AC on the cardiac SPECT images, and the AC-SPECT

using the ProMap were evaluated against the AC-SPECT images corrected with CTMap using RE%, MSE, and SSIM and statistical analysis of 17 segmental average values of myocardial counts. All continuous values were expressed as mean ± SD. The paired t-test was applied to determine statistically significant differences in the quantitative values; p values <0.05 were considered significant. GraphPad InStat version 3.06 for Windows (GraphPad Software, San Diego, CA, USA) and SPSS software (23.0; SPSS Inc.) was used for statistical analysis. Segmental values of the databases were expressed as the average and SD, which were calculated by QPS software.

Results

Patient Studies-reconstructed Images

Table 1 shows the mean, and SD of the MSE, and SSIM between the proposed attenuation maps and the CT attenuation maps. Among the generated attenuation maps, the lowest mean error metrics were resulted in the males' attenuation map, which are MSE: 0.06±1.11. The highest error metrics of males (MSE: 0.08 and 0.21 for rest and stress respectively). The highest error metrics of females (MSE: 0.11 and 0.10 for rest and stress respectively). The mean of SSIM for females were 0.92±0.02 for stress and 0.93±0.01 for rest, respectively, and for males 0.96±0.01 for stress and 0.97±0.02 for rest, respectively.

Clinical myocardial perfusion image (MPI) SPECT/CT data were used as a means of validating the proposed attenuation map approach compared with direct AC using a CT attenuation map. The qualitative analysis of the comparison between two attenuation maps was checked and approved by a well-experienced nuclear medicine physician.

Table 2 shows that the intraclass correlation coefficient for quantitative tracer uptake of images reconstructed using the synthesized attenuation map and CT-based attenuation map for attenuation-corrected images; the correlation coefficients for males were 0.93 [95% confidence interval (CI), 0.91-0.95] for stress images and 0.95 (95% CI, 0.93-0.96) for rest images and for females were 0.87 (95% CI,

0.84-0.89) for stress images and 0.92 (95% CI, 0.91-0.94) for rest images.

Although the clinical assessment of the method was not within the scope of our study in this phase, the impact of AC on clinical images was observed in some cases. Two sample studies male and female of reconstructed images from a SPECT myocardial perfusion study with and without AC using CTMap and ProMap are shown in Figure 1. The two patients were 73 and 62-year-old man and woman, respectively, were presenting with chest pain. The figure display depicts that without AC, low uptake in the in the inferior, inferoseptal, and inferolateral walls can be observed (yellow arrows), while this region becomes more homogeneous with AC using either CTMap or ProMap. Moreover, the result was interpreted as negative for appreciable stress-induced ischemia.

The CT-based attenuation maps, and proposed attenuation maps in the axial, coronal, and sagittal views at the upper left, MPI SPECT reconstructed images corrected using CT-based attenuation maps, proposed method and without AC in short axis, horizontal long axis and vertical long axis views and the polar map comparisons are shown in Figure 1.

The proposed method could generate consistent attenuation maps with the standard CT-based attenuation maps. The upper right images in Figure 1 for each subject show that the myocardial perfusion SPECT reconstructed images corrected using the CT-based attenuation map and the proposed attenuation map have good consistent, whereas obvious attenuation artifacts can be observed in the non-attenuation-corrected images, as pointed by

Table 2. Percentage segmental tracer uptake: correlation between proposed AC method and CT based AC method

AC				
	Male		Female	
Phase	R	95% CI	r	95% CI
Stress	0.93	0.91-0.95	0.87	0.84-0.89
Rest	0.95	0.93-0.96	0.92	0.91-0.94

r: Correlation coefficient, CI: Confidence interval, AC: Attenuation correction

Table 1. The mean and SD of the mean square error one, and structural similarity index measure one between proposed attenuation maps and the CT attenuation maps and MSE2 and SSIM2 between non-attenuation corrected image and proposed attenuation corrected image

Metric	MSE1				MSE2				SSIM1				SSIM2			
	Female		Male		Female		Male		Female		Male		Female		Male	
	Stress	Rest	Stress	Rest	Stress	Rest	Stress	Rest	Stress	Rest	Stress	Rest	Stress	Rest	Stress	Rest
Mean	0.07	0.07	0.07	0.06	0.23	0.21	0.20	0.19	0.92	0.93	0.96	0.97	0.69	0.75	0.77	0.79
SD	0.002	0.007	0.004	0.001	0.012	0.03	0.01	0.02	0.020	0.010	0.010	0.020	0.10	0.09	0.08	0.05

SD: Standard deviation, MSE: Mean square error one, SSIM: Similarity index measure, CT: Computed tomography

the yellow arrows. The 17-segment polar maps for each subject in Figure 1 (generated by Cedars-Sinai software package) of the SPECT images corrected by both CT-based and proposed attenuation maps are nearly consistent. In contrast, the polar maps without AC clearly show different patterns.

The new proposed method was also tested with the patients having fixed defects. Figure 2 shows that the proposed attenuation map works well not only with normal perfusion patients but also with patients having fixed defects. As shown in Figure 2 our result reveal that the proposed new

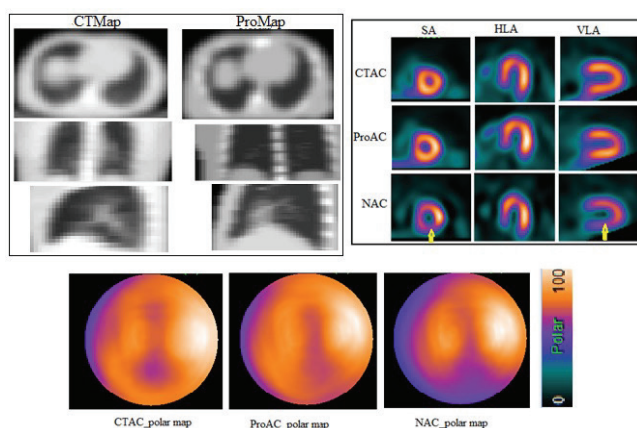


Figure 1. a) A 73-year-old male normal patient. b) A 62-year-old female, both have reversible cardiac perfusion defect in the right coronary arteries NAC: Non-attenuation correction, CTAC: Computed tomography based attenuation correction, ProAC: Proposed attenuation correction, SA: Short axis, HLA: Horizontal long axis, VLA: Vertical long axis

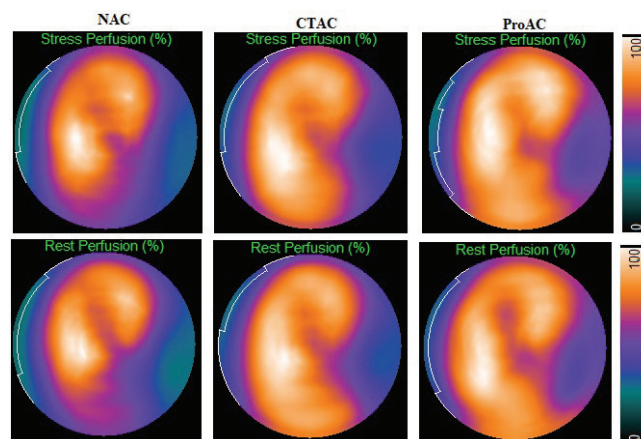


Figure 2. Polar plot presentation of nuclear myocardial perfusion images from a male with fixed left circumflex artery perfusion defect with attenuation (CTAC and ProAC) and without attenuation (NAC) on standard SPECT/CT camera

NAC: Non-attenuation correction, CTAC: Computed tomography based attenuation correction, ProAC: Proposed attenuation correction, SPECT/CT: Single-photon emission computed tomography/computed tomography

method for cardiac AC is even better than the CT-based AC. This might be because of the potential misregistration of SPECT and CT data because of they are obtained sequentially. Possible risk factors for misregistration include improper patient positioning, respiratory motion, patient motion, or mechanical misalignment of SPECT/CT device. To reduce this problem, before generating the results, the authors cross checked and corrected manually. Moreover, after applying ProMAP and CTMap for AC our finding showed that quantitatively better regional radiotracer distribution in the inferior, septal, and anterior walls with the new method than the CTMap-based method.

Polar plot presentation of nuclear MPIs from a male with a fixed left circumflex artery perfusion defect with attenuation (ProAC and CTAC) and NAC on a standard SPECT/CT camera.

Homogeneity of Cardiac Images with and Without AC

Figure 3 shows the mean PV of circumferential count profiles from short-axis patients images acquired with NAC, ProAC, and CTAC. With ProAC and CTAC the percent variability of circumferential count profiles was significantly reduced in both genders, indicating greater image homogeneity. The mean \pm SD values for females were $(8.0 \pm 0.96\%$ and $7.6 \pm 0.8072\%)$ for CTAC, $(7.99 \pm 0.07\%$ and $7.90 \pm 1.25\%)$ for ProAC and $(10.67 \pm 1.02\%$ and $10.07 \pm 1.60\%)$ for NAC, respectively, for stress and rest. The measures for males were CTAC $(6.8 \pm 1.17\%$, $7.1 \pm 0.63\%)$, ProAC $(7.6 \pm 0.98\%$, $7.2 \pm 0.79\%)$ and, $(10.16 \pm 0.69\%$, $9.24 \pm 0.9\%)$ respectively for stress and rest. There were statistically significant differences between ProAC and NAC values for females-

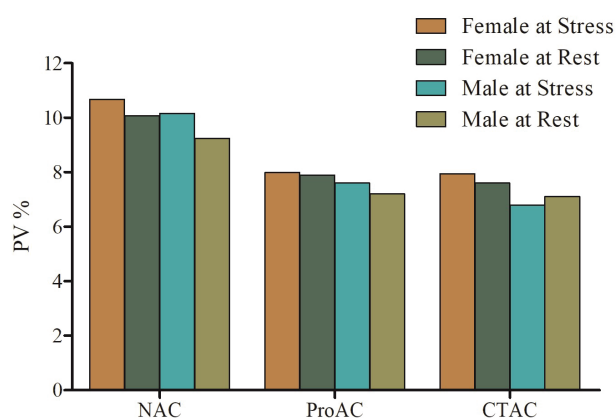


Figure 3. Circumferential percent variability, as a measure for image homogeneity, in basal, mid and apical regions. Percent variability improved significantly with the application of cardiac SPECT images with ProAC and CTAC compared with NAC

NAC: Non-attenuation correction, CTAC: Computed tomography based attenuation correction, ProAC: Proposed attenuation correction, SPECT: Single-photon emission computed tomography

stress and males-stress ($p=0.034$ and $p=0.036$), respectively, and there were statistically significant differences between CTAC and NAC for females-stress and males-stress ($p=0.010$ and $p=0.035$), respectively. Only for male stress that a significant difference between CTAC and ProAC ($p=0.035$) was observed.

Further quantitative analysis of the cardiac region was conducted by examining the percentage of RE% in the segmental region. Figure 4 shows box plots for the percentage of RE% of each segmental region between the ProAC and CTAC images for the cardiac regions across both genders. The graph shows that there was no significant median difference between the proposed AC and the standard transmission-based AC except in apical-anterior region in females in the rest phase ($p<0.0001$). 82% of male and 76% of female patients had studies where there was a segmental difference between ProAC and CTAC of less than ± 5 .

Statistical Differences in Database Analysis

In Table 3, clinical SPECT/CT data were used as a means of validating the ProMap approach compared with direct AC using CTMap and calculated segmental average and SD values in 17-segment models for stress, and rest are

shown. Figure 5 shows perfusion polar maps reconstructed images with and without AC using CTMap and ProMap. After applying AC as revealed on the polar maps, uniform count distribution was observed when the inferior and anterolateral counts were compared

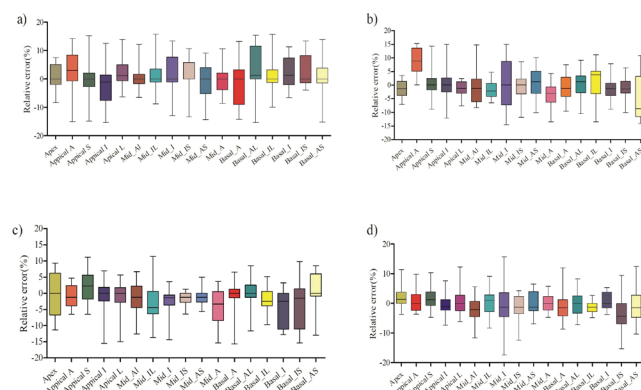


Figure 4. Box and whisker plots along with relative error percentage between images processed with ProAC and CTAC which were calculated for 17 segments of myocardial regions: a) female-stress, b) female-rest, c) male-stress, d) male-rest respectively
ProAC: Proposed attenuation correction, CTAC: Computed tomography based attenuation correction

Table 3. Segmental average and standard deviation values in the polar maps with non-attenuation correction, proposed attenuation correction and CT-based attenuation correction

	NAC				ProAC				CTAC			
	Stress		Rest		Stress		Rest		Stress		Rest	
	Female	Male	Female	Male	Female	Male	Female	Male	Female	Male	Female	Male
Apex	82±7.60	80±7.10	81±8.40	79±7.10	81±7.55	79±6.2	78±7.72	83±6.30	82±6.40	79 ±6.64	78±7.34	81±5.70
Apical-A	77±7.44	74±7.28	77±8.40	72±7.90	79±7.81	82±7.90	84±5.44	83±4.59	77±6.14	83±4.31	77±5.36	82±4.80
Apical-S	84±7.84	77±9.40	78±6.52	76±10.00	86±6.41	88±5.70	84±5.70	88±7.74	86±6.34	85±5.61	83±6.01	86±5.62
Apical-I	80±7.30	74±8.40	83±8.24	78±8.30	86±6.92	84±6.14	80±6.41	84±7.91	84±6.60	85±5.60	80±6.74	82±7.42
Apical-L	76±9.10	77±9.70	78±6.80	78±6.11	82±5.84	87±6.92	82±4.82	86±6.21	84±5.90	88±5.11	83±4.26	85±5.80
Mid-AL	78±6.63	77±7.08	81±6.80	74±9.10	85±5.70	88±5.00	87±5.33	87±7.30	86±5.41	89±4.50	88±6.30	88±7.30
Mid-IL	78±8.90	76±8.20	79±6.80	79±8.01	84±5.04	82±6.30	88±4.27	88±7.20	87±4.50	85±7.20	89±5.44	88±5.41
Mid-I	80±10.1	71±6.81	85±8.11	73±6.30	82±8.20	82±5.60	84±8.50	84±5.60	88±7.10	84±6.20	84±8.83	84±6.40
Mid-IS	80±7.20	71±8.30	78±4.12	72±6.20	85±7.20	80±5.80	85±6.50	81±5.00	84±5.40	79±6.33	85±6.90	81±5.44
Mid-AS	75±6.04	75±6.70	76±3.20	73±5.30	81±6.58	82±6.12	81±8.31	80±4.50	81±6.31	83±6.00	80±7.53	80±5.80
Mid-A	77±8.10	73±6.60	77±6.90	77±4.43	78±7.83	86±3.05	73±7.74	85±6.67	78±7.33	86±3.64	76±7.80	85±6.09
Basal-A	68±8.62	70±6.23	68±7.73	70±8.50	78±4.40	79±6.02	72±5.60	79±7.39	77±7.50	79±5.91	72±6.92	79±8.20
Basal-AL	72±8.02	68±9.91	71±6.24	69±9.50	74±6.91	80±5.41	78±6.61	78±5.30	77±8.01	89±6.03	78±8.20	79±6.02
Basal-IL	72±7.50	67±10.10	72±6.29	68±9.33	74±5.10	74±6.54	79±6.43	75±5.90	75±7.13	76±5.81	78±4.70	76±6.00
Basal-I	70±7.40	62±5.73	68±7.73	64±5.90	76±4.80	67±7.50	77±6.81	73±6.50	78±6.80	72±6.03	78±6.84	72±6.20
Basal-IS	68±7.91	62±6.40	67±8.04	65±6.90	72±6.16	64±6.60	72±6.61	65±5.91	75±6.83	67±7.10	73±4.70	68±5.60
Basal-AS	62±7.12	64±8.20	65±7.30	64±7.70	65±6.70	66±7.00	62±8.44	66±5.80	66±7.50	65±6.70	66±5.01	66±5.41

A: Anterior, S: Septal, L: Lateral, AL: Anterolateral, IL: Inferolateral, IS: Inferoseptal, AS: Anteroseptal, I: Inferior, NAC: Non-attenuation correction, ProAC: Proposed attenuation correction, CTAC: Computed tomography based attenuation correction, CT: Computed tomography

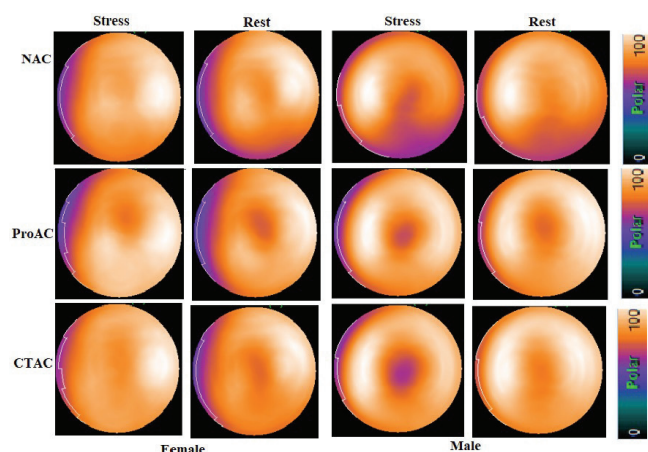


Figure 5. Comparison of the polar maps for NAC, ProAC and CTAC in female and male. The differences in the lateral and inferior counts between AC and NAC are shown

NAC: Non-attenuation correction, CTAC: Computed tomography based attenuation correction, ProAC: Proposed attenuation correction, AC: Attenuation correction

Paired t-test results for the comparison of ProAC and CTAC are shown in Table 4. As it was revealed, in the most cardiac regions, there is no significant difference between the two methods, which indicates that our proposed method is consistent with the standard method (CT based cardiac AC).

A paired sample t-test demonstrated that counts in the apical-lateral, mid-inferolateral, mid-anterolateral, mid-inferoseptal, basal-inferior, and basal-anterolateral were significantly higher than NAC in both genders and in both AC methods (Table 5). With AC using CTMap and ProMap, there were counted decreases in the apex for both genders but only CTAC female rest was statistically significant ($p < 0.0001$).

Regarding the gender difference analysis, for the stress condition basal-inferior and inferoseptal showed significant differences in all ProAC ($p = 0.001$ and $p = 0.001$), CTAC ($p < 0.0001$ and $p = 0.015$), and NAC ($p = 0.006$ and $p = 0.006$) respectively. Moreover, mid-anterior during the rest condition showed a significant difference between male and females in ProAC ($p < 0.0001$) and in CTAC ($p = 0.001$ and $p = 0.001$) during stress and rest conditions, respectively. This might be caused by the anatomical difference between females and males.

Discussion

In this study, we proposed an effective method for generating an attenuation map directly from emission data using the segmentation of non-rigid registration of XCAT digital anatomical phantom with the emission image and assigning the tissue-based density map. Validation on real

patient studies revealed that the proposed method can generate attenuation maps nearly consistent with CT-based attenuation maps and were able to provide accurate AC for myocardial perfusion SPECT images. Also, in most of the regions, no significant segmental average values of myocardial count differences were observed between ProMap and CTMap (Table 4). This finding could be important for the studies acquired with dedicated cardiac SPECT or SPECT standalone scanners by providing AC without transmission data.

In Figure 5, it can be seen that our proposed AC achieved moreover similar results compared to the currently used standard approach. The proposed method reduced attenuation artifacts and changed the calculated segmental average values of myocardial counts compared with NAC databases. When AC is implemented optimally, the spread of radionuclide for the lateral, inferior and anterior and lastly septum received higher to lower perfusion. The attenuation-

Table 4. p values for comparison of proposed AC (ProAC) versus CT-based AC (CTAC)

	P values for comparison of ProAC and CTAC			
	Stress		Rest	
	Female	Male	Female	Male
Apex	ns	ns	ns	ns
Apical-A	ns	<0.0001	ns	ns
Apical-S	ns	ns	ns	ns
Apical-I	ns	ns	ns	ns
Apical-L	ns	ns	ns	ns
Mid-AL	ns	ns	ns	ns
Mid-IL	ns	ns	ns	ns
Mid-I	ns	ns	ns	ns
Mid-IS	ns	ns	0.008	ns
Mid-AS	ns	ns	ns	ns
Mid-A	ns	0.001	ns	ns
Basal-A	ns	ns	ns	ns
Basal-AL	ns	ns	ns	ns
Basal-IL	ns	ns	ns	0.014
Basal-I	ns	ns	ns	ns
Basal-IS	0.016	ns	ns	ns
Basal-AS	ns	ns	ns	ns

A: Anterior, S: Septal, L: Lateral, AL: Anterolateral, IL: Inferolateral, IS: Inferoseptal, AS: Anteroseptal, I: inferior, NAC: Non-attenuation correction, ProAC: Proposed attenuation correction, CTAC: Computed tomography based attenuation correction, CT: Computed tomography, ns: Not significant, AC: Attenuation correction

Table 5. p values in comparison NAC, ProAC and CTAC

	P values for female versus male						p values for NAC versus ProAC						p values for NAC versus CTAC					
	NAC		ProAC		CTAC		Stress		Rest		Stress		Rest		Stress		Rest	
	Stress	Rest	Stress	Rest	Stress	Rest	Stress	Rest	Stress	Rest	Stress	Rest	Stress	Rest	Stress	Rest	Stress	Rest
Apex	ns	ns	0.014	<0.0001	0.003	0.004	ns	ns	ns	ns	ns	ns	ns	ns	ns	ns	<0.0001	ns
Apical-A	ns	ns	ns	ns	<0.0001	0.01	ns	ns	0.001	0.001	<0.0001	<0.0001	<0.0001	<0.0001	ns	<0.0001	ns	<0.0001
Apical-S	ns	ns	ns	0.039	ns	ns	ns	ns	0.002	0.004	<0.0001	<0.0001	<0.0001	ns	0.005	0.006	0.001	0.001
Apical-H	0.023	ns	ns	0.013	ns	ns	ns	0.009	<0.0001	ns	0.034	0.035	<0.0001	ns	<0.0001	ns	ns	ns
Apical-L	ns	ns	0.009	ns	0.023	ns	ns	0.004	0.002	0.031	0.001	0.001	0.001	<0.0001	<0.0001	0.012	<0.0001	<0.0001
Mid-AL	ns	ns	ns	ns	0.030	ns	ns	0.001	0.002	0.001	0.006	<0.0001	<0.0001	<0.0001	<0.0001	<0.0001	<0.0001	0.003
Mid-IL	ns	ns	ns	ns	ns	ns	ns	0.004	0.010	<0.0001	<0.0001	0.004	<0.0001	<0.0001	<0.0001	<0.0001	<0.0001	<0.0001
Mid-I	ns	<0.0001	ns	ns	ns	ns	ns	ns	<0.0001	ns	<0.0001	0.02	<0.0001	ns	<0.0001	ns	<0.0001	<0.0001
Mid-IS	0.025	0.008	0.035	ns	0.023	ns	ns	0.039	<0.0001	0.005	<0.0001	0.01	<0.0001	<0.0001	0.008	<0.0001	<0.0001	<0.0001
Mid-AS	0.004	ns	ns	ns	0.028	ns	ns	<0.0001	<0.0001	0.033	0.001	0.047	<0.0001	<0.0001	ns	0.003	0.003	0.003
Mid-A	ns	ns	ns	<0.0001	0.001	0.001	0.001	ns	0.001	<0.0001	0.001	ns	ns	<0.0001	ns	0.001	0.001	0.001
Basal-A	ns	ns	ns	0.005	ns	ns	ns	<0.0001	<0.0001	ns	<0.0001	<0.0001	<0.0001	<0.0001	<0.0001	0.033	0.01	0.01
Basal-AL	ns	ns	ns	ns	ns	ns	ns	0.02	<0.0001	<0.0001	0.001	0.031	<0.0001	<0.0001	<0.0001	<0.0001	<0.0001	<0.0001
Basal-IL	ns	ns	ns	ns	ns	ns	ns	ns	<0.0001	0.001	0.010	ns	<0.0001	<0.0001	<0.0001	0.001	0.004	0.004
Basal-I	0.006	ns	0.001	ns	0.002	0.018	0.015	<0.0001	<0.0001	<0.0001	<0.0001	<0.0001	<0.0001	<0.0001	<0.0001	<0.0001	<0.0001	<0.0001
Basal-IS	0.006	0.010	0.001	0.006	0.001	0.015	0.015	0.005	<0.0001	0.004	ns	0.049	<0.0001	<0.0001	0.002	0.002	0.002	0.002
Basal-AS	ns	ns	ns	ns	ns	ns	ns	0.006	<0.0001	ns	ns	0.008	<0.0001	<0.0001	ns	0.041	0.041	0.041

A: Anterior, S: Septal, L: Lateral, AL: Anterolateral, IL: Inferolateral, IS: Inferoseptal, AS: Anteroseptal, I: Inferior, NAC: Non-attenuation correction, ProAC: Proposed attenuation correction, CTAC: Computed tomography based attenuation correction, CI: Computed tomography, ns: Not significant, AC: Attenuation correction

corrected myocardial perfusion counts using both ProMap and CTMap were more homogeneous than NAC images and the anterolateral, inferolateral and inferior counts were increased. We found an increase inhomogeneity in females than men after AC was applied. This is in agreement with the observations of Masood et al. (11). Moreover, to apply the proposed AC for clinical use, there is a need for creating attenuation-corrected databases for quantitative analysis.

MPIs most often suffer from attenuation artifacts in males and females due to attenuation from the diaphragm and breast (37,38). Although the clinical assessment of the proposed method was not within the scope of our study in this phase, there is a positive influence of AC on these attenuation artifacts. Figure 6, shows stress-only MPI performed with SPECT/CT in a female patient (body mass index 31 kg/m²) shows a large clear perfusion defect in the anterolateral myocardial wall (arrows) on images obtained without attenuation correction (NAC), whereas attenuation-corrected images (ProAC) show no evidence of a defect at this site (arrowheads). These findings indicate a soft-tissue attenuation artifact that was eliminated with AC.

There were significant differences with and without AC average count in the inferior region for males (which is expected where diaphragm attenuation artifact is prominent, p=<0.0001 and <0.0001) and basal-antrolateral for females (where breast attenuation artifact prominent, p=0.02 and <0.0001) for stress and rest, respectively. This result is promising in terms of improving attenuation artifacts in the inferior segment in males and anterior segments in females because it provides a homogeneous count distribution in both genders. In a CT-based AC study by Grossman et al. (39), AC polar maps increased global uniformity of the count distribution.

As expected, there were significant count distribution differences between ProAC

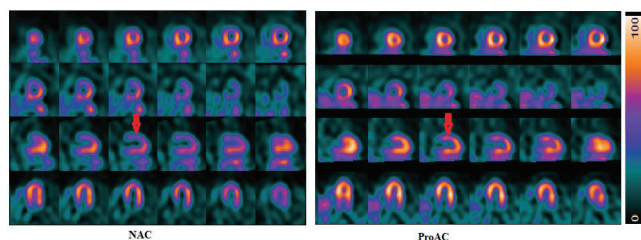


Figure 6. Images obtained without attenuation correction (NAC) and with attenuation-correction (ProAC) and the effect of soft tissue attenuation artifact for large density breast was eliminated with the proposed attenuation correction

NAC: Non-attenuation correction, ProAC: Proposed attenuation correction

and NAC and between CTAC and NAC with stress and rest conditions for both genders. In most of the regions, both AC methods showed that gender differences were not statistically significant, which is consistent with the finding of Grossman et al. (39). However, our technique created a slightly higher bias on female subjects than male subjects, which is agreement with the finding of Shi et al. (1). This might be caused by the anatomical difference between females and males.

In our study, the quantitative analysis performed using MSE, and SSIM to assess the consistence of the proposed attenuation map with CT-based attenuation map (Table 1). The range of absolute RE in any 17 segmental region did not exceed 15%. More or less the percentage of RE was consistent over all regions.

The overall benefit of AC in clinical cardiac SPECT was beyond the scope of the current study. We expect a limited benefits in increasing the quality and quantitative analysis in the diagnosis of CAD. Moreover, avoiding the necessity of CT data for AC reduces the radiation exposure risk to the patient. The proposed method of AC is not intended to replace CT but rather to be viewed as a valid alternative when CT is not available. Also, there may be suspicious drawbacks concerning the reduction of accuracies in real clinical cases due to smearing or over correction, which should be further addressed in future clinical applications of the proposed AC method.

Study Limitations

Our study has several limitations: precisely registration of an XCAT digital phantom with emission image and assignment of attenuation values to the right region is not an easy task. Although non-homogeneous density of body tissue needs to assign continuous attenuation values, discrete attenuation coefficients are used for segmented XACT-emission image non-rigid registration-based AC. Therefore, analyzing the interindividual irregularity of tissue density and its effect on AC in cardiac SPECT is an

imperative issue. Moreover, an important limitation of this study is the interpatient variability of attenuation values, which can be the main cause of error in cardiac SPECT emission data. Mainly, based on the risk factors such as age, disease, and breathing patterns, lung density shows a high degree of interpatient variability of up to 10% (40). Image reconstruction and registration method used to obtain the final attenuation corrected of SPECT emission images also affect the final result.

Conclusion

The proposed attenuation maps show good agreement with the CT-based attenuation map. AC is feasible for myocardial perfusion SPECT images by only emission data as an alternative to the AC by CT-derived attenuation map. This could direct benefit studies acquired with dedicated cardiac SPECT or SPECT standalone scanners. There were significant count differences between ProAC and NAC, and the homogeneity of radioactivity distribution was increased with ProAC. Further studies in patients with CAD should be conducted to evaluate the clinical efficacy of the proposed AC method.

Ethics

Ethics Committee Approval: The study was approved by the Vice-Chancellor in Research Affairs-Tehran University of Medical Sciences (27/11/2018).

Informed Consent: All patients gave their informed consent before inclusion in the study.

Peer-review: Internally peer-reviewed.

Authorship Contributions

Surgical and Medical Practices: G.F.T., P.G., M.R.A., Concept: M.R.A., P.G., M.A., Design: G.F.T., E.M.T., M.A., A.S, Data Collection or Processing: G.F.T., M.M., M.A., A.S., Analysis or Interpretation: G.F.T., P.G., M.A., B.T., M.R.A., Literature Search: G.F.T., M.M., P.G., B.T., Writing: G.F.T., P.G., M.R.A.

Conflict of Interest: No conflict of interest was declared by the authors.

Financial Disclosure: The authors want to acknowledge Tehran University of Medical Sciences (TUMS) for providing materials support during this project implementation under grant No. 38086. We would also like to acknowledge all the patients whose data were used in this study, and all the healthcare workers who took part in the diagnosis of included patients. We also acknowledge Parto Negar Persia (PNP) Co. for providing technical material and Co.

References

1. Shi L, Onofrey JA, Liu H, Liu YH, Liu C. Deep learning-based attenuation map generation for myocardial perfusion SPECT. *Eur J Nucl Med Mol Imaging* 2020;47:2383-2395.
2. Yamauchi Y, Kanzaki Y, Otsuka K, Hayashi M, Okada M, Nogi S, Morita H, Komori T, Ishizaka N. Novel attenuation correction of SPECT images

- using scatter photopeak window data for the detection of coronary artery disease. *J Nucl Cardiol* 2014;21:109-117.
3. van Dijk JD, Mouden M, Ottervanger JP, van Dalen JA, Knollema S, Slump CH, Jager PL. Value of attenuation correction in stress-only myocardial perfusion imaging using CZT-SPECT. *J Nucl Cardiol* 2017;24:395-401.
 4. Patchett ND, Pawar S, Sverdlow A, Miller EJ. Does improved technology in SPECT myocardial perfusion imaging reduce downstream costs? An observational study. *Int J Radiol Imaging Technol* 2017;3.
 5. King MA, Tsui BM, Pan TS. Attenuation compensation for cardiac single-photon emission computed tomographic imaging: Part 1. Impact of attenuation and methods of estimating attenuation maps. *J Nucl Cardiol* 1995;2:513-524.
 6. King MA, Tsui BM, Pan TS, Glick SJ, Soares EJ. Attenuation compensation for cardiac single-photon emission computed tomographic imaging: part 2. Attenuation compensation algorithms. *J Nucl Cardiol* 1996;3:55-64.
 7. Manglos SH, Jaszczak RJ, Floyd CE, Hahn LJ, Greer KL, Coleman RE. Nonisotropic attenuation in SPECT: phantom tests of quantitative effects and compensation techniques. *J Nucl Med* 1987;28:1584-1591.
 8. Tsui BM, Gullberg GT, Edgerton ER, Ballard JG, Perry JR, McCartney WH, Berg J. Correction of nonuniform attenuation in cardiac SPECT imaging. *J Nucl Med* 1989;30:497-507.
 9. Zaidi H, Hasegawa B. Determination of the attenuation map in emission tomography. *J Nucl Med* 2003;44:291-315.
 10. Abdollahi H, Shiri I, Salimi Y, Sarebani M, Mehdinia R, Deevband MR, Mahdavi SR, Sohrabi A, Bitarafan-Rajabi A. Radiation dose in cardiac SPECT/CT: an estimation of SSDE and effective dose. *Eur J Radiol* 2016;85:2257-2261.
 11. Masood Y, Liu YH, Depuey G, Taillefer R, Araujo LI, Allen S, Delbeke D, Anstett F, Peretz A, Zito MJ, Tsatkin V, Wackers FJ. Clinical validation of SPECT attenuation correction using X-ray computed tomography-derived attenuation maps: multicenter clinical trial with angiographic correlation. *J Nucl Cardiol* 2005;12:676-686.
 12. Rahman A, Zhu Y, Clarkson E, Kupinski MA, Frey EC, Jha AK. Fisher information analysis of list-mode SPECT emission data for joint estimation of activity and attenuation distribution. *Inverse Probl* 2020;36:084002.
 13. <https://www.technavio.com/report/global-medical-imaging-global-spectmarket-2017-2021>. Accessed 5 Nov 2019.
 14. Fard BT, Sabet KA, Ay M. Introducing a dedicated cardiac SPECT imaging system: ProSPECT. *Frontiers in Biomedical Technologies* 2019;6:156-160.
 15. Zeraatkar N, Sajedi S, Fard BT, Kaviani S, Akbarzadeh A, Farahani MH, Sarkar S, Ay MR. Development and calibration of a new gamma camera detector using large square Photomultiplier Tubes. *J Instrum* 2017;12:P09008.
 16. Cade SC, Arridge S, Evans MJ, Hutton BF. Use of measured scatter data for the attenuation correction of single photon emission tomography without transmission scanning. *Med Phys* 2013;40:082506.
 17. Núñez M, Prakash V, Vila R, Mut F, Alonso O, Hutton BF. Attenuation correction for lung SPECT: evidence of need and validation of an attenuation map derived from the emission data. *Eur J Nucl Med Mol Imaging* 2009;36:1076-1089.
 18. Pan TS, King MA, De Vries DJ, Ljungberg M. Segmentation of the body and lungs from Compton scatter and photopeak window data in SPECT: a Monte-Carlo investigation. *IEEE Trans Med Imaging* 1996;15:13-24.
 19. Pan TS, King MA, Luo DS, Dahlberg ST, Villegas BJ. Estimation of attenuation maps from scatter and photopeak window single photon-emission computed tomographic images of technetium 99m-labeled sestamibi. *J Nucl Cardiol* 1997;4:42-51.
 20. Gourion D, Noll D, Gantet P, Celler A, Esquerré JP. Attenuation correction using SPECT emission data only. *IEEE Trans Nucl Sci* 2002;49:2172-2179.
 21. Krol A, Bowsheer JE, Manglos SH, Feiglin DH, Tornai MP, Thomas FD. An EM algorithm for estimating SPECT emission and transmission parameters from emission data only. *IEEE Trans Med Imaging* 2001;20:218-232.
 22. Nuyts J, Dupont P, Stroobants S, Binninck R, Mortelmans L, Suetens P. Simultaneous maximum a posteriori reconstruction of attenuation and activity distributions from emission sinograms. *IEEE Trans Med Imaging* 1999;18:393-403.
 23. Rahman A, Zhu Y, Clarkson E, Kupinski MA, Frey EC, Jha AK. Fisher information analysis of list-mode SPECT emission data for joint estimation of activity and attenuation distribution. *Inverse Probl* 2020;36:084002.
 24. Yan Y, Zeng GL. Attenuation map estimation with SPECT emission data only. *Int J Imaging Syst Technol* 2009;19:271.
 25. Segars WP, Sturgeon G, Mendonca S, Grimes J, Tsui BM. 4D XCAT phantom for multimodality imaging research. *Med Phys* 2010;37:4902-4915.
 26. Segars WP, Bond J, Frush J, Hon S, Eckersley C, Williams CH, Feng J, Tward DJ, Ratnanather JT, Miller MI, Frush D, Samei E. Population of anatomically variable 4D XCAT adult phantoms for imaging research and optimization. *Med Phys* 2013;40:043701.
 27. Segars WP, Mahesh M, Beck TJ, Frey EC, Tsui BM. Realistic CT simulation using the 4D XCAT phantom. *Med Phys* 2008;35:3800-3808.
 28. Segars WP, Tsui BMW, Jing Cai, Fang-Fang Yin, Fung GSK, Samei E. Application of the 4-D XCAT Phantoms in Biomedical Imaging and Beyond. *IEEE Trans Med Imaging* 2017;37:680-692.
 29. Okuda K, Nakajima K, Motomura N, Kubota M, Maeda H, Matsuo S, Kinuya S. Attenuation correction of myocardial SPECT by scatter-photopeak window method in normal subjects. *Ann Nucl Med* 2009;23:501-506.
 30. Lange K, Bahn M, Little R. A theoretical study of some maximum likelihood algorithms for emission and transmission tomography. *IEEE Trans Med Imaging* 1987;6:106-114.
 31. Lange K, Carson R. EM reconstruction algorithms for emission and transmission tomography. *J Comput Assist Tomogr* 1984;8:306-316.
 32. Shepp LA, Vardi Y. Maximum likelihood reconstruction for emission tomography. *IEEE Trans Med Imaging* 1982;1:113-122.
 33. King MA, Glick SJ, Pretorius PH, Wells RG, Gifford HC, Narayanan MV, Farncombe T. Attenuation, scatter, and spatial resolution compensation in SPECT. *Emission tomography: the fundamentals of PET and SPECT*. Academic 2004, 473-498.
 34. Gullberg GT, Huesman RH, Malko JA, Pelc NJ, Budinger T. An attenuated projector-backprojector for iterative SPECT reconstruction. *Phys Med Biol* 1985;30:799-816.
 35. Ay MR, Shirmohammad M, Sarkar S, Rahmim A, Zaidi H. Comparative assessment of energy-mapping approaches in CT-based attenuation correction for PET. *Mol Imaging Biol* 2011;13:187-198.
 36. Zeintl J, Vija AH, Yahil A, Hornegger J, Kuwert T. Quantitative accuracy of clinical 99mTc SPECT/CT using ordered-subset expectation maximization with 3-dimensional resolution recovery, attenuation, and scatter correction. *J Nucl Med* 2010;51:921-928.
 37. Munn S. The way to a man's heart is through his stomach: much "diaphragmatic" attenuation is likely gastric, and effervescent granules enhance cardiac imaging. *Eur J Radiol* 2004;52:271-275.
 38. Goodgold HM, Rehder JG, Samuels LD, Chaitman BR. Improved interpretation of exercise Tl-201 myocardial perfusion scintigraphy in women: characterization of breast attenuation artifacts. *Radiology* 1987;165:361-366.
 39. Grossman GB, Garcia EV, Bateman TM, Heller GV, Johnson LL, Folks RD, Cullom SJ, Galt JR, Case JA, Santana CA, Halkar RK. Quantitative Tc-99m sestamibi attenuation-corrected SPECT: development and multicenter trial validation of myocardial perfusion stress gender-independent normal database in an obese population. *J Nucl Cardiol* 2004;11:263-272.
 40. Keereman V, Van Holen R, Mollet P, Vandenberghe S. The effect of errors in segmented attenuation maps on PET quantification. *Med Phys* 2011;38:6010-6019.